The Astrophysical Journal Letters, 861:L8 (7pp), 2018 July 1 https://doi.org/10.3847/2041-8213/aaccef

Neutron-capture Elements in Planetary Nebulae: First Detections of Near-infrared [Te III] and [Br V] Emission Lines*†

Simone Madonna[1,2], Manuel Bautista[3], Harriet L. Dinerstein[4], N. C. Sterling[5], Jorge García-Rojas[1,2], Kyle F. Kaplan[4,6], Maria del Mar Rubio-Díez[7], Nieves Castro-Rodríguez[1,2,8], and Francisco Garzón[1,2]
[1] Instituto de Astrofísica de Canarias, E-38200, La Laguna, Tenerife, Spain; smadonna@iac.es
[2] Universidad de La Laguna. Depart. de Astrofísica, E-38206, La Laguna, Tenerife, Spain
[3] Department of Physics, Western Michigan University, Kalamazoo, MI 49008, USA
[4] Department of Astronomy, University of Texas, 2515 Speedway, C1400, Austin, TX 78712-1205, USA
[5] Department of Physics, University of West Georgia, 1601 Maple Street, Carrollton, GA 30118, USA
[6] Department of Astronomy & Steward Observatory, 933 North Cherry Avenue, University of Arizona, Tucson, AZ 85721-0065, USA
[7] Centro de Astrobiología, CSIC-INTA, Carretera de Torrejón a Ajalvir, km 4, E-28850 Torrejón de Ardoz, Spain
[8] GRANTECAN, Cuesta de San José s/n, E-38712 , Breña Baja, La Palma, Spain
Received 2018 May 28; revised 2018 June 9; accepted 2018 June 12; published 2018 June 28

Abstract

We have identified two new near-infrared (NIR) emission lines in the spectra of planetary nebulae arising from heavy elements produced by neutron-capture reactions: [Te III] 2.1019 μm and [Br V] 1.6429 μm. [Te III] was detected in both NGC 7027 and IC 418, while [Br V] was seen in NGC 7027. The observations were obtained with the medium-resolution spectrograph Espectrógrafo Multiobjeto Infra-Rojo (EMIR) on the 10.4 m Gran Telescopio Canarias at La Palma, and with the high-resolution Immersion GRating INfrared Spectrometer (IGRINS) on the 2.7 m Harlan J. Smith telescope at McDonald Observatory. New calculations of atomic data for these ions, specifically A-values and collision strengths, are presented and used to derive ionic abundances of Te^{2+} and Br^{4+}. We also derive ionic abundances of other neutron-capture elements detected in the NIR spectra, and estimate total elemental abundances of Se, Br, Kr, Rb, and Te after correcting for unobserved ions. Comparison of our derived enrichments to theoretical predictions from asymptotic giant branch (AGB) evolutionary models shows reasonable agreement for solar metallicity progenitor stars of $\sim$2–4 $M_{\odot}$. The spectrally isolated [Br V] 1.6429 μm line has advantages for determining nebular Br abundances over optical [Br III] emission lines that can be blended with other features. Finally, measurements of Te are of special interest because this element lies beyond the first peak of the *s*-process, and thus provides new leverage on the abundance pattern of trans-iron species produced by AGB stars.

Key words: atomic data – line: identification – nuclear reactions, nucleosynthesis, abundances – planetary nebulae: individual (IC 418, NGC 7027) – stars: AGB and post-AGB

1. Introduction

Nucleosynthetic processes in asymptotic giant branch (AGB) stars produce a substantial fraction of the trans-iron ($Z > 30$) elements present in the Solar System and the universe. During the late thermally pulsing AGB evolutionary stage of low- and intermediate-mass ($\sim$1.5–8 $M_{\odot}$) stars, iron peak nuclei in the intershell region between the He- and H-burning shells experience sequential neutron(*n*)-captures interlaced with β decays, forming heavier elements via the so-called slow neutron capture or "*s*-process." The free neutrons are released as a result of alpha captures by ^{13}C or ^{22}Ne nuclei during phases of the thermal pulse cycle (Käppeler et al. 2011). Convective dredge-up from the intershell region (third dredge-up (TDU)) may convey *s*-processed material, along with C, to the stellar surface, which is released into the interstellar medium by stellar winds and planetary nebula (PN) ejection (Karakas & Lattanzio 2014, and references therein).

PNe are valuable laboratories for studying the *s*-process because they represent the final envelope compositions of their progenitor stars after the last thermal pulse and cessation of nucleosynthesis and TDU. The past few years have seen rapid development of near-infrared (NIR) spectroscopy as a tool for such investigations. The first NIR emission lines of *n*-capture elements discovered, [Kr III] 2.199 μm and [Se IV] 2.287 μm (Dinerstein 2001), have been widely observed in Milky Way and Magellanic Cloud PNe (Sterling & Dinerstein 2008; Sterling et al. 2015; hereafter SPD15; Mashburn et al. 2016). Additional NIR line detections include [Rb IV], [Cd IV], [Ge VI], [Se III], and [Kr VI] (Sterling et al. 2016, 2017).

In this Letter we present the discovery of NIR lines from the *n*-capture elements Br and Te, and the atomic data needed to derive chemical abundances from the line intensities. Although optical lines of Te^{2+} and Br^{2+} have previously been reported in some PNe (Péquignot & Baluteau 1994; Sharpee et al. 2007; hereafter SH07; Madonna et al. 2017; hereafter MGR17), they are faint and potentially blended with lines of other species. The discovery of relatively bright NIR lines of these *n*-capture elements provides an important new opportunity for determining the contributions of AGB stars to galactic enrichment.

2. Observations and Data Reduction

2.1. Espectrógrafo Multiobjeto Infra-Rojo (EMIR) Observations

We observed the PNe IC 418 and NGC 7027 with the NIR spectrograph EMIR (Garzón et al. 2006, 2014) on the 10.4 m Gran Telescopio Canarias at the Roque de los Muchachos

* This Letter includes data taken at The McDonald Observatory of The University of Texas at Austin.

† This Letter includes observations made with the Gran Telescopio Canarias (GTC), installed in the Spanish Observatorio del Roque de los Muchachos of the Instituto de Astrofsica de Canarias, on the island of La Palma. Program ID GTC8-17AESCIVER.

Table 1
Journal of Observations

Instrument	$\Delta\lambda$ (μm)	$\lambda/\Delta\lambda$	t_{exp} (s)	Date
NGC 7027				
EMIR	1.17–1.33	4800	720	2016 Oct 18
"	1.52–1.77	4500	720	"
"	2.03–2.37	4000	720	"
IGRINS	1.45–2.45	45000	1080	2014 Oct 24
IC 418				
EMIR	2.03–2.37	3500	360	2017 Oct 5
IGRINS	1.45–2.45	45000	2400	2015 Nov 2

Observatory, La Palma. The observations were carried out during commissioning and science verification runs of EMIR in longslit mode ($6\farcs7 \times 0\farcs8$ for IC 418 and $6\farcs7 \times 0\farcs6$ for NGC 7027), delivering spectral resolutions $R \sim 3500$ in K for IC 418, and $R \sim 4800$, 4500, and 4000 in J, H, and K, respectively, for NGC 7027. The slit was oriented north to south (N–S) and centered on the central star of IC 418. For NGC 7027 the slit was centered on the eastern ridge at coordinates (R.A., decl., J2000) $21^h07^m02\fs16$, $+42°14'10\farcs3$, and was rotated to a position angle of 105° east of N–S to intersect the peak of the western ridge. We nodded 50″ along the slit for both objects to optimize observing efficiency. A0V standard stars were observed and used for spectrophotometric flux calibration for each PN. We also used the standard star to correct for telluric absorption for IC 418, but for NGC 7027 we used a synthetic atmosphere spectrum calculated with ATRAN tools[9] due to a large airmass difference between the PN and its standard star. Wavelength calibration was performed using HgAr lamp spectra. The basic data reduction was carried out with IRAF, while we used MarTell (M. del Mar Rubio-Díez et al. 2018, in preparation) to perform the telluric absorption correction. Line fluxes were measured using the *splot* routine in IRAF by integrating the flux above the local continuum. Table 1 presents a journal of the observations.

2.2. Immersion GRating INfrared Spectrometer (IGRINS) Observations

Both targets were also observed with IGRINS on the Cassegrain focus on the 2.7 m Harlan J. Smith Telescope at McDonald Observatory (Table 1). IGRINS is a NIR cross-dispersed echelle spectrometer that uses a silicon immersion grating to achieve high spectral resolving power, $R \sim 45000$, with instantaneous complete coverage from 1.45–2.45 μm (Park et al. 2014). The fixed long slit has dimensions of $1'' \times 15''$ on the sky and was rotated to a position angle 60° east of N–S for NGC 7027, so that it intersected the peaks of both the eastern and western ridges. For IC 418, the slit was oriented N–S and centered $3\farcs5$ west of the central star. All observations were taken in a nod-off-slit pattern with sky frames at least 30″ from the source position. Standard A0V stars observed at similar airmasses as the PNe were employed for telluric correction and spectrophotometric flux calibration. The data reduction and analysis were performed as described in Kaplan et al. (2017).

[9] https://atran.sofia.usra.edu/cgi-bin/atran/atran.cgi

3. Identification of [Te III] 2.1019 μm and [Br V] 1.6429 μm

Table 3 presents the intensities of NIR n-capture element lines as ratios to nearby H I lines, and Figure 1 shows excerpts of the spectral regions near the features that we identify as [Te III] and [Br V]. While the lines are unresolved in the EMIR data, their profiles as seen with IGRINS reflect actual velocity structure and are consistent with the profiles of other ionic lines. Because the ionization potential (IP) of Te^+ is 18.55 eV and that of Te^{2+} is 27.96 eV, a significant fraction of the Te in PNe with cool central stars, such as IC 418, should be in the form of Te^{2+}. Despite its hotter central star, the bright, s-process enriched PN NGC 7027 also shows [Te III]. Because stellar photons of at least 47.24 eV are required to produce Br^{4+}, it is not surprising that we do not see [Br V] in IC 418.

We identify the line near 2.1019 μm as the $5s^25p^2\ ^3P_1$–$^3P_0$ transition of Te^{2+}. Although the most recently reported vacuum laboratory value is 2.1021 μm (Tauheed & Naz 2011), the IGRINS observations indicate that the actual wavelength is 2.1019 μm, in good accord with the experimental data of Joshi et al. (1992). The older energy level values of Moore (1958) correspond to a wavelength of 2.1048 μm. This highlights the importance of ongoing atomic physics research, especially laboratory spectroscopy, for identifying n-capture element transitions, as well the value of high-spectral resolution astronomical observations for measuring precise wavelengths.

We considered alternate identifications within ±10Å of the detected features by querying the Atomic Line List v2.05b21.[10] One of the most plausible alternate identifications is [Fe II] 2.1017 μm. However, other [Fe II] lines of the same multiplet are not detected, although they are predicted to be brighter than this transition according to calculations with PyNeb v1.0.26 (Luridiana et al. 2015). Additionally, the feature at 2.1017 μm is too strong by several orders of magnitude to be consistent with the Fe^+ ionic abundance derived from [Fe II] 1.2570, 12946, and 1.6440 μm. An even closer wavelength coincidence with the observed feature is 4s $^2P_{1/2}$–$^4P_{1/2}$ [Ni II] 2.1019 μm, one of several transitions that can be enhanced over the strength expected for pure collisional excitation by UV continuum fluorescence (Bautista et al. 1996). We eliminated this possibility as several other [Ni II] transitions that are expected to be strong under such excitation conditions (1.7249, 1.7651, 2.0492, and 2.0811 μm) are not detected.

Additional supporting evidence for the identification of the 2.1019 μm line as [Te III] is the consistency of Te^{2+} ionic abundances derived from this line with values based on [Te III] λ7933.31. From the flux of this line in IC 418 reported by Sharpee et al. (2003), we find a Te^{2+} abundance within ~0.2 dex of that from the NIR line (see Table 3). There is only an upper limit on the intensity of [Te III] λ7933.31 in NGC 7027 (SH07), but this is consistent with our results as the corresponding limit on the Te^{2+} abundance is larger than the value that we derive from [Te III] 2.1019 μm (Table 3).

We identify the line at 1.6429 μm seen in NGC 7027 as the $4s^24p\ ^2P^o_{3/2} - {}^2P^o_{1/2}$ transition of Br^{4+}, for which the energy levels provided by Riyaz et al. (2014) yield a vacuum wavelength of 1.6429 μm. We searched the Atomic Line List and found no plausible alternate atomic lines. $H_2\ 6-4\ Q(5)$, which can be strong in sources with highly fluorescent H_2 spectra (K. F. Kaplan et al. 2018, in preparation), is a potential

[10] http://www.pa.uky.edu/~peter/newpage/

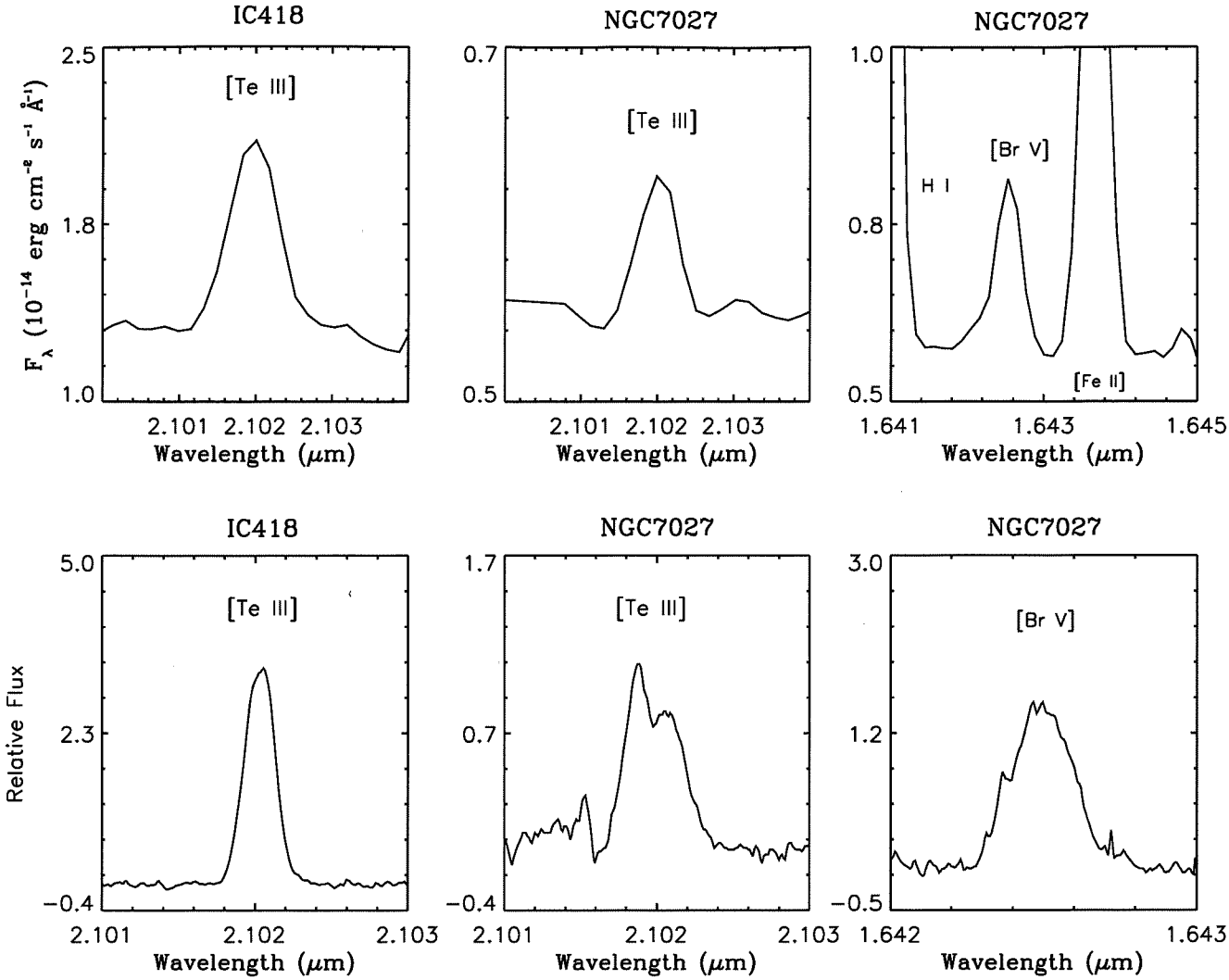

Figure 1. Plots of the newly detected lines from the EMIR (upper row) and IGRINS (lower row) data. While the EMIR line fluxes were measured from their 1D spectra, the IGRINS fluxes were measured in 2D position–velocity space with an aperture drawn around the line profile (e.g., see Figure 1 of Sterling et al. 2016).

contaminant, but the IGRINS data demonstrate that it is not present at a detectable intensity.

The good agreement between EMIR and IGRINS results and the high resolution of IGRINS data, which eliminates the possibility of blends, give us confidence that [Te III] and [Br V], respectively, are the correct identifications for the 2.1019 μm and 1.6429 μm lines.

4. A-values and Collision Strengths

The atomic structures, A-values, and radial wavefunctions for Br V and Te III were computed with the AUTOSTRUCTURE code Badnell (1986, 1997). We diagonalized the Breit–Pauli Hamiltonian within a statistical Thomas–Fermi–Dirac–Amaldi model potential $V(\lambda_{nl})$ (Badnell 1997). The potential for each orbital was characterized by scaling the radial parameter by a quantity λ_{nl} that is optimized variationally by minimizing a weighted sum of the *LS* term energies. The *LS* terms are represented by configuration-interaction (CI) wavefunctions.

The CI expansion for the Br V system that we used includes the $3d^{10}4s^24p$, $3d^{10}4s4p^2$, $3d^{10}4s^25s$, $3d^{10}4s^25p$, $3d^{10}4s^25d$, $3d^94s^24p^2$, $3d^94s^24p4d$, and $3d^94s^24p5s$ configurations, while that for Te III includes $4d^{10}5s^25p^2$, $4d^{10}5s5p^3$, $4d^{10}5s^25p5d$, and $4d^95s^25p^3$.

The quality of our atomic structure representations was evaluated by comparing predicted term energies with the experimental values of Riyaz et al. (2014) and Joshi et al. (1992) for Br V and Te III, respectively. Our calculated energies are found to differ from experimental values by less than 5%. Additional small semi-empirical corrections to the orbitals were calculated through the coupling of energy terms that minimized the relative energy differences. Finally, the level energies were shifted to the experimental values in order to compute monopole, dipole, and quadrupole transition probabilities.

The scattering calculations were done with the BP *R*-matrix program (Berrington et al. 1997), using the orbitals from our AUTOSTRUCTURE calculation, retaining CI from 39 *LS* terms and 88 fine structure levels for Br V and 39 *LS* terms and 75 levels for Te III. The calculations explicitly include partial waves from states with $L \leqslant 9$ and multiplicities 1, 3, and 5 for Br V, and 2 and 4 for Te III. Contributions from the higher partial waves were estimated using a top-up procedure.

Maxwellian-averaged collision strengths were computed for both ions for selected temperatures between 5000 K and 30000 K. New atomic data files with the resulting values for Br V and Te III were added to PyNeb. The A-values and

Table 2
A-values and Collision Strengths

Transition	$A_{ij}[s^{-1}]$	$\Upsilon(T)$ 5000 K	8000 K	10000 K	15000 K	20000 K	30000 K
				Te^{2+}			
$^3P_1-^3P_0$	1.194	5.812	4.965	4.553	3.848	3.4	2.848
$^3P_2-^3P_0$	1.209E–02	2.565	2.597	2.62	2.652	2.642	2.561
$^1D_2-^3P_0$	1.062E–04	1.08	1.1	1.103	1.082	1.045	0.9653
$^1S_0-^3P_0$	...	0.1534	0.159	0.1626	0.1694	0.1721	0.1696
$^3P_2-^3P_1$	0.52	8.74	8.487	8.403	8.255	8.085	7.684
$^1D_2-^3P_1$	5.141	4.317	4.43	4.463	4.421	4.297	4.004
$^1S_0-^3P_1$	6.797E+01	0.6048	0.632	0.6414	0.6502	0.6452	0.6158
$^1D_2-^3P_2$	5.266	8.606	8.86	8.924	8.896	8.749	8.368
$^1S_0-^3P_2$	7.098	1.053	1.177	1.222	1.271	1.273	1.228
$^1S_0-^1D_2$	7.902	4.021	3.949	3.915	3.855	3.818	3.763
				Br^{4+}			
$^2P^0_{3/2}-^2P^0_{1/2}$	0.991	5.39	5.014	4.908	4.892	5.055	5.507
$^2D_{3/2}-^2P^0_{1/2}$	1.507E+06	0.932	0.771	0.7088	0.6186	0.568	0.5084
$^2D_{5/2}-^2P^0_{1/2}$	4.920E+04	0.8377	0.7848	0.7679	0.7479	0.7355	0.7109
$^2P_{1/2}-^2P^0_{1/2}$	...	0.8529	0.8508	0.8575	0.8684	0.8653	0.8371
$^2P_{3/2}-^2P^0_{1/2}$	7.741E+08	3.292	3.208	3.179	3.138	3.112	3.069
$^2D^0_{3/2}-^2P^0_{1/2}$	...	1.505	1.585	1.633	1.708	1.733	1.707
$^2D^0_{5/2}-^2P^0_{1/2}$	2.694E+09	1.488	1.446	1.423	1.385	1.368	1.359
$^2D_{3/2}-^2P^0_{3/2}$	4.842E+05	1.522	1.244	1.14	0.9867	0.8946	0.7781
$^2D_{5/2}-^2P^0_{3/2}$	6.594E+05	1.601	1.549	1.536	1.502	1.458	1.368
$^2P_{1/2}-^2P^0_{3/2}$	2.146E+06	2.128	2.291	2.336	2.341	2.287	2.152
$^2P_{3/2}-^2P^0_{3/2}$	6.632E+07	2.793	2.618	2.571	2.514	2.476	2.397
$^2D^0_{3/2}-^2P^0_{3/2}$	7.471E+08	7.551	7.202	7.062	6.833	6.68	6.461
$^2D^0_{5/2}-^2P^0_{3/2}$	1.313E+09	1.586	1.525	1.482	1.402	1.357	1.313
$^2D_{5/2}-^2D_{3/2}$	0.129	4.457	3.822	3.521	3.027	2.735	2.424
$^2P_{1/2}-^2D_{3/2}$	2.285E–04	2.666	2.34	2.215	2.026	1.912	1.785
$^2P_{3/2}-^2D_{3/2}$	0.666	0.6057	0.5456	0.5272	0.5109	0.5135	0.5339
$^2D^0_{3/2}-^2D_{3/2}$	2.818E–03	0.3996	0.3728	0.3685	0.3783	0.4003	0.4478
$^2D^0_{5/2}-^2D_{3/2}$	9.839	0.1252	0.1689	0.1908	0.2288	0.2531	0.282
$^2P_{1/2}-^2D_{5/2}$	0.277	7.721	6.645	6.211	5.539	5.147	4.744
$^2P_{3/2}-^2D_{5/2}$	2.092	0.7815	0.7616	0.763	0.7834	0.8142	0.8767
$^2D^0_{3/2}-^2D_{5/2}$	1.531	1.294	1.16	1.119	1.09	1.106	1.174
$^2D^0_{5/2}-^2D_{5/2}$	38.414	0.2605	0.3401	0.38	0.448	0.4907	0.5414
$^2P_{3/2}-^2P_{1/2}$	0.780	1.142	1.008	0.9629	0.9157	0.9126	0.9448
$^2D^0_{3/2}-^2P_{1/2}$	5.646	2.394	2.123	2.032	1.929	1.903	1.924
$^2D^0_{5/2}-^2P_{1/2}$	1.190	0.2343	0.3052	0.355	0.4641	0.547	0.6547
$^2D^0_{3/2}-^2P_{3/2}$	0.0002	3.196	3.405	3.512	3.693	3.796	3.879
$^2D^0_{5/2}-^2P_{3/2}$	21.699	1.437	1.402	1.383	1.351	1.334	1.323
$^2D^0_{5/2}-^2D^0_{3/2}$	30.410	2.151	2.047	1.995	1.919	1.885	1.864

Maxwellian-averaged collision strengths are presented in Table 2.

5. Elemental Abundances and Enrichments

We recalculated the physical conditions, and ionic and elemental abundances of O, S, and Ar that are used in our abundance analysis, using PyNeb and line fluxes from multi-wavelength studies of IC 418 (Bernard Salas et al. 2001; Pottasch et al. 2004) and NGC 7027 (Zhang et al. 2005). Multi-wavelength observations provide access to multiple ions per element, which minimizes systematic uncertainties due to the contributions of unobserved ions. We take the total elemental abundances of O in IC 418, and of Ar and S in both PNe, to be equal to the sum of all observed ionic abundances. For the high-excitation PN NGC 7027, we correct for the presence of unobserved O^{4+} using the formula from Delgado-Inglada et al. (2014). The atomic data used and the treatment of uncertainties are the same from the literature. The two sets of *n*-capture abundances agree to within 0.1 dex in all cases.

5.1. Elemental Abundances of Te and Br

The determination of elemental from ionic abundances requires correction for unobserved ionization stages. A widely used approach for such corrections is to construct formulae that define ionization correction factors (ICFs), where the ICF is the inverse of the fractional abundance of the element in the observed ion(s). ICF prescriptions are most reliable when based on photoionization models that account for the radiative and

Table 3
n-capture Ionic and Elemental Abundances

Line (μm) Ratio	Flux Ratio	$\log(X^{i+}/H^{+})+12$	Ionization Correction Factor[a]	$\log(X/H)+12$[a] This Work	$\log(X/H)+12$[b]
NGC 7027 ($T_e = 12450 \pm 600$ K, $n_e = 50500^{+25700}_{-14600}$ cm^{-3})					
EMIR					
[Se IV] 2.2864/Brγ	0.0919 ± 0.0055	3.20 ± 0.04	2.52 ± 1.12	3.60 ± 0.16	3.56 ± 0.14
[Br V] 1.6429/Br11	0.0295 ± 0.0021	2.23 ± 0.05	2.80 ± 0.56	2.67 ± 0.06	2.72 ± 0.06
[Kr III] 2.1986/Brγ	0.0329 ± 0.0023	3.40 ± 0.04	1.32 ± 0.25	4.13 ± 0.08	4.11 ± 0.08
[Kr VI] 1.2330/Pβ	0.0078 ± 0.0005	2.55 ± 0.04	...	...	...
[Rb IV] 1.5973/Br11	0.0335 ± 0.0023	2.86 ± 0.05	1.58 ± 0.33	3.06 ± 0.09	3.03 ± 0.09
[Te III] 2.1019/Brγ	0.0030 ± 0.0008	1.50 ± 0.11	17.28 ± 2.94	2.74 ± 0.12	2.64 ± 0.12
IGRINS					
[Se IV] 2.2864/Brγ	0.0835 ± 0.0083	3.16 ± 0.05	2.52 ± 1.12	3.56 ± 0.17	3.52 ± 0.14
[Br V] 1.6429/Br11	0.0245 ± 0.0049	2.15 ± 0.08	2.80 ± 0.56	2.59 ± 0.09	2.64 ± 0.09
[Kr III] 2.1986/Brγ	0.0307 ± 0.0031	3.38 ± 0.05	1.32 ± 0.25	4.12 ± 0.09	4.10 ± 0.08
[Rb IV] 1.5973/Br11	0.0290 ± 0.0029	2.80 ± 0.06	1.58 ± 0.33	3.00 ± 0.10	2.97 ± 0.10
[Te III] 2.1019/Brγ	0.0031 ± 0.0003	1.51 ± 0.05	17.28 ± 2.94	2.75 ± 0.07	2.65 ± 0.07
Literature[c]					
[Te III] 0.7933/Hβ	<0.002	<2.15	...	...	...
IC418 ($T_e = 8670 \pm 250$ K, $n_e = 13650^{+8200}_{-3400}$ cm^{-3})					
EMIR					
[Se IV] 2.2864/Brγ	0.0019 ± 0.0008	1.72 ± 0.15	5.81 ± 2.14	2.48 ± 0.19	2.46 ± 0.18
[Kr III] 2.1986/Brγ	0.0258 ± 0.0015	3.51 ± 0.03	1.82 ± 0.32	3.77 ± 0.06	3.77 ± 0.06
[Te III] 2.1019/Brγ	0.0122 ± 0.0011	2.29 ± 0.04	2.58 ± 0.31	2.70 ± 0.07	2.67 ± 0.07
IGRINS					
[Se IV] 2.2864/Brγ	0.0014 ± 0.0001	1.57 ± 0.04	5.81 ± 2.14	2.33 ± 0.14	2.31 ± 0.14
[Kr III] 2.1986/Brγ	0.0262 ± 0.0026	3.51 ± 0.04	1.82 ± 0.32	3.77 ± 0.07	3.77 ± 0.07
[Te III] 2.1019/Brγ	0.0126 ± 0.0013	2.31 ± 0.04	2.58 ± 0.31	2.72 ± 0.07	2.69 ± 0.07
Literature[d]					
[Te III] 0.7933/Hβ	0.0017	2.53	...	...	...

Notes.
[a] Results from our abundance re-calculations. For details of the adopted ionization correction factors (ICFs), see Section 5.1.
[b] Calculated using values for physical conditions and for ionic and total abundances of light elements from the literature (see Section 5.1).
[c] Sharpee et al. (2007).
[d] Sharpee et al. (2003).

collisional processes that affect the ionization balance of each element (Delgado-Inglada et al. 2014, SPD15), but such models require atomic data for photoionization and recombination processes. When these data are unknown, as is the case for Br and Te ions, approximate ICFs can be estimated using coincidences in IPs with ions of more abundant elements. However, these approximate ICFs are much more uncertain than those derived from photoionization models.

To convert the measured ionic into elemental abundances for NGC 7027 and IC 418, we assumed that $\mathrm{Te/Ar} = \mathrm{Te}^{2+}/\mathrm{Ar}^{+}$ and $\mathrm{Br/Ar} = \mathrm{Br}^{4+}/\mathrm{Ar}^{3+}$, based on similarities between the IP ranges of those ions. Adopting these procedures, we find Te abundances in both PNe that are higher than solar by a factor of ~3.5, while Br is modestly (if at all) enhanced in NGC 7027.

5.2. Abundances of Other n-capture Elements

Elemental abundances of other *n*-capture elements detected in the EMIR and IGRINS spectra of NGC 7027 and IC 418 are also given in Table 3. For NGC 7027, we calculate the Kr total abundance using the ICF value of Sterling et al. (2017) which incorporates lines of four ions. For IC 418, we used Equation (1) of SPD15, which uses the $\mathrm{S}^{2+}/\mathrm{S}$ ratio and is based on Kr^{2+} only, but the higher ions should not be prevalent in this low-ionization PN. The Rb abundance in NGC 7027 was calculated assuming $\mathrm{Rb/O} = \mathrm{Rb}^{3+}/\mathrm{O}^{2+}$, as in Sterling et al. (2016). For both PNe we computed the Se abundance using the ICF given by Equation (8) of SPD15.

In Column 2 of Table 4 we list the averaged values from the EMIR and IGRINS data for the total abundances of the *n*-capture elements. Column 3 reports the enhancements of these abundances relative to the solar values of Asplund et al. (2009). We adopt the meteoritic abundances for all but Kr, which is based on solar wind measurements and interpolation from other elements (see Section 3.9.5 of Asplund et al. 2009).

Column 4 summarizes previous determinations of the elemental enrichments based on NIR emission lines, which

Table 4
n-capture Element Enrichments

Element	Elemental Abundances[a]	$[X/H]$[b]	$[X/H]$[c]
	NGC 7027		
Se	3.58 ± 0.17	0.24 ± 0.17	0.34 ± 0.10
Br	2.64 ± 0.08	0.10 ± 0.10	
Kr	4.13 ± 0.09	0.88 ± 0.11	0.85 ± 0.04
Rb	3.03 ± 0.10	0.67 ± 0.10	0.70 ± 0.20
Te	2.75 ± 0.10	0.57 ± 0.10	
	IC 418		
Se	2.40 ± 0.17	−0.94 ± 0.17	<−0.32
Kr	3.77 ± 0.07	0.52 ± 0.09	0.50 ± 0.20
Te	2.71 ± 0.07	0.53 ± 0.08	

Notes.
[a] Average from EMIR and IGRINS results.
[b] $\log(X/H)_{PN}$–$\log(X/H)_{\odot}$.
[c] Literature abundances for NGC 7027 from Sterling et al. (2016) and Sterling et al. (2017); those for IC 418 are from SPD15.

agree within uncertainties with the values reported here. While Sterling et al. (2016) compared their Rb abundance with the photospheric solar Rb value of 2.52, after adjusting to the meteoritic value of 2.36 their abundance corresponds to an enhancement of [Rb/H] = 0.70, which is in excellent agreement with the current result. The Se abundance that we find for IC 418, nearly a factor of 10 below solar, is not consistent with the paradigm of self-enrichment by the *s*-process. However, in this low-excitation PN, most of the Se atoms will be in the form of Se^{2+}, which we have not observed, making the correction to the Se^{3+} abundance large and uncertain (Table 3). In addition, Sterling et al. (2017) suggested that the currently employed Se/Se^{3+} ICF may break down in low- to moderate-excitation PNe, highlighting the importance of measuring the J-band [Se III] 1.0994 μm line first reported by these authors.

5.3. Comparison to Theoretical Models of AGB Evolution

Enrichments of *n*-capture elements have been predicted by several groups that model AGB evolution and nucleosynthesis. The resulting abundance patterns are similar for progenitor masses $M < 4$–$5\ M_{\odot}$, while the absolute enrichments tend to vary between different sets of models and even for different treatments of the physics by the same group. We have compared our results with the final abundances calculated by Karakas & Lugaro (2016) and Cristallo et al. (2015) for solar metallicity (Z = 0.014) AGB stars, as our recalculated O abundances are near the solar value (12 + log(O/H) = 8.69 for NGC 7027, 8.62 for IC 418). While the former models predict higher enrichments overall and are in better agreement with our measurements, the relative enrichments of the observed elements are generally consistent with both sets of models for initial masses of 2–$4\ M_{\odot}$. Our observations agree with the predictions that the enrichments of Kr and Rb are larger than those of Se and Br. The enrichment of Te changes little ($\leqslant$0.2 dex) over this mass range, while the elements Se–Rb show greater variations. We do not find Te to be enriched more strongly than Kr as predicted by the models, but this may be due to uncertainties in our approximate Te ICF. The enrichments for NGC 7027 are consistent with a progenitor initial mass of around $3 \pm 0.5\ M_{\odot}$ as estimated by Zhang et al. (2005) and other studies (see Sterling et al. 2016, for references). The Kr enrichment of IC 418 suggests a lower mass for its progenitor star, which has been estimated as $M = 1.75\ M_{\odot}$ (Morisset & Georgiev 2009) and as $M = 1.4 \pm 0.5\ M_{\odot}$ (Henry et al. 2018).

5.4. Abundances and Origins of Br and Te in Astronomical Sources

Br and Te are difficult to detect in stars, particularly in giants, because their strongest neutral transitions lie in the UV where red giants emit little flux.

Large enhancements of Br have been reported in HgMn stars (e.g., Cowley & Wahlgren 2006) and He-rich DO white dwarfs (Werner et al. 2018), but these are attributed to chemical stratification due to diffusion and radiative levitation that result in photospheric abundances unrepresentative of overall composition. Faint optical lines of Br^{2+} have previously been reported in six PNe (Péquignot & Baluteau 1994, SH07, MGR17). However, [Br III] λ6130.37 can be blended with C III λ6130.30 (García-Rojas et al. 2015), and the unrealistically large Br abundances derived from [Br III] λ6555.56 (SH07, MGR17) led MGR17 to suggest that this line may be contaminated by an unknown feature. While SH07 tentatively identified [Br IV] λ7368.00 and λ9450.50 in NGC 7027, they question these identifications owing to uncertainties in the continuum level and the possible presence of instrumental ghosts. Therefore, at present the NIR [Br V] line is the most reliable indicator of Br abundances in high-excitation nebulae.

Te has been detected in HgMn stars (Cowley et al. 2006), DO white dwarfs (e.g., Rauch et al. 2017; Hoyer et al. 2018), and metal-poor halo stars (e.g., Roederer et al. 2014). The Te abundances in the halo stars are consistent with a scaled solar *r*-process distribution, indicating little or no *s*-process enrichment. While approximately 80% of the solar system Te abundance was formed in the *r*-process (Bisterzo et al. 2011), ^{122}Te, ^{123}Te, and ^{124}Te are *s*-only isotopes that are produced in low-mass AGB stars (Takahashi et al. 2016).

Thus PNe represent the only viable means of studying Te in one of its sites of origin, with one intriguing exception. Smartt et al. (2017) obtained optical and NIR data of the kilonova AT 2017gfo associated with the neutron star merger event GW170817, and tentatively identified lines of Te I in the early-time spectrum. Unfortunately, the Te abundance could not be determined, due to the lack of reliable oscillator strengths and the fact that Te II is expected to be the dominant ion. Nevertheless, this possible detection, and that of lanthanides in neutron star mergers, provide motivation to study the production of *n*-capture elements in all their sites of origin, in order to better constrain models of galactic chemical evolution.

S.M. and J.G.R. acknowledge support from the Spanish Ministerio de Economía y Competividad under projects AYA2015-65205-P and AYA2017-83383-P. M.A.B. and N.C.S. acknowledge support from NSF award AST-1412928, and H.L.D. from AST-1715332. J.G.R. acknowledges support from the Severo Ochoa excellence program (SEV-2015-0548). This work used IGRINS, developed by the University of Texas at Austin and the Korea Astronomy and Space Science Institute (KASI) with the financial support of NSF grant AST-1229522, the University of Texas at Austin, and the Korean GMT Project

of KASI. This work has made use of the NASA Astrophysics Data System.

ORCID iDs

Manuel Bautista https://orcid.org/0000-0001-6837-3055
Harriet L. Dinerstein https://orcid.org/0000-0002-4017-5572
N. C. Sterling https://orcid.org/0000-0002-9604-1434
Jorge García-Rojas https://orcid.org/0000-0002-6138-1869

Kyle F. Kaplan https://orcid.org/0000-0001-6909-3856
Nieves Castro-Rodríguez https://orcid.org/0000-0002-4269-0279
Francisco Garzón https://orcid.org/0000-0002-0971-5024

References

Asplund, M., Grevesse, N., Sauval, A. J., & Scott, P. 2009, ARA&A, 47, 481
Badnell, N. R. 1986, JPhB, 19, 3827
Badnell, N. R. 1997, JPhB, 30, 1
Bautista, M. A., Peng, J., & Pradhan, A. 1996, ApJ, 460, 372
Bernard Salas, J., Pottasch, S. R., Beintema, D. A., & Wesselius, P. R. 2001, A&A, 367, 949
Berrington, K. A., Burke, P. F., Butler, K., et al. 1997, JPhB, 20, 6379
Bisterzo, S., Gallino, R., Straneiro, O., Cristallo, S., & Käppeler, F. 2011, MNRAS, 418, 284
Cowley, C. R., Hubrig, S., González, G. F., & Nuñez, N. 2006, A&A, 455, L21
Cowley, C. R., & Wahlgren, G. M. 2006, A&A, 447, 681
Cristallo, S., Straniero, O., Piersanti, L., & Gobrecht, D. 2015, ApJS, 219, 40
Delgado-Inglada, G., Morisset, C., & Stasińska, G. 2014, MNRAS, 440, 536
Dinerstein, H. L. 2001, ApJL, 550, L223
García-Rojas, J., Madonna, S., Luridiana, V., et al. 2015, MNRAS, 452, 2606
Garzón, F., Abreu, D., Barrera, S., et al. 2006, Proc. SPIE, 6269, 626918
Garzón, F., Castro-Rodríguez, N., Insausti, M., et al. 2014, Proc. SPIE, 9147, 0U
Henry, R. B. C., Stephenson, B. G., Miller Bertolami, M. M., Kwitter, K. B., & Balick, B. 2018, MNRAS, 473, 241
Hoyer, D., Rauch, T., Werner, K., & Kruk, J. W. 2018, A&A, 612, A62
Joshi, Y. N., Tauheed, A., & Davidson, I. G. 1992, CaJPh, 70, 740
Kaplan, K. F., Dinerstein, H. L., Oh, H., et al. 2017, ApJ, 838, 152
Käppeler, F., Gallino, R., Bisterzo, S., & Aoki, W. 2011, RvMP, 83, 157
Karakas, A. I., & Lattanzio, J. C. 2014, PASA, 31, 62
Karakas, A. I., & Lugaro, M. 2016, ApJ, 825, 26
Luridiana, V., Morisset, C., & Shaw, R. A. 2015, A&A, 573, A42
Madonna, S., García-Rojas, J., Sterling, N. C., et al. 2017, MNRAS, 471, 1341, (MGR17)
Mashburn, A. L., Sterling, N. C., Madonna, S., et al. 2016, ApJL, 831, L3
Moore, C. E. 1958, Atomic Energy Levels, Vol. 3 (Washington, DC: U.S. Government Printing Office) National Bureau of Standards Circular No. 467
Morisset, C., & Georgiev, L. 2009, A&A, 507, 1517
Park, C., Jaffe, D. T., Yuk, I.-S., et al. 2014, Proc. SPIE, 9147, 91471D
Péquignot, D., & Baluteau, J.-P. 1994, A&A, 283, 593
Pottasch, S. R., Bernard-Salas, J., Beintema, D. A., & Faibelman, W. A. 2004, A&A, 423, 593
Rauch, T., Quinet, P., Knörzer, M., et al. 2017, A&A, 606, A105
Riyaz, A., Tauheed, A., & Rahimullah, K. 2014, JQSRT, 147, 86
Roederer, I. U., Schatz, H., Lawler, J. E., et al. 2014, ApJ, 791, 32
Sharpee, B., Williams, R., Baldwin, J. A., & van Hoof, P. A. M. 2003, ApJS, 149, 157
Sharpee, B., Zhang, Y., Williams, R., et al. 2007, ApJ, 659, 1265, (SH07)
Smartt, S. J., Chen, T.-W., Jerkstrand, A., et al. 2017, Natur, 551, 75
Sterling, N. C., & Dinerstein, H. L. 2008, ApJS, 174, 158
Sterling, N. C., Dinerstein, H. L., Kaplan, K. F., & Bautista, M. A. 2016, ApJ, 819, 9
Sterling, N. C., Madonna, S., Butler, K., et al. 2017, ApJL, 840, 80
Sterling, N. C., Porter, R. L., & Dinerstein, H. L. 2015, ApJS, 218, 25, (SPD15)
Takahashi, K., Blaum, K., & Novikov, Yu. 2016, ApJ, 819, 118
Tauheed, A., & Naz, A. 2011, JKPS, 59, 2910
Werner, K., Rauch, T., Knörzer, M., & Kruk, J. W. 2018, A&A, in press (arXiv:1803.04809)
Zhang, Y., Liu, X.-W., Luo, S.-G., Péquignot, D., & Barlow, M. J. 2005, A&A, 442, 249